Anisotropic phase diagram of ferroquadrupolar ordering in the trigonal chiral compound DyNi₃Ga₉

Isao Ishii,[*] Kohki Takezawa, Takuyou Mizuno, Soichiro Kumano, and Takashi Suzuki[†]
Department of Quantum Matter, AdSM, Hiroshima University, Higashi-Hiroshima 739-8530, Japan

Hiroki Ninomiya
*Electronics and Photonics Research Institute, National Institute of Advanced Industrial Science and Technology,
Tsukuba, Ibaraki 305-8568, Japan*

Keisuke Mitsumoto
Liberal Arts and Sciences, Faculty of Engineering, Toyama Prefectural University, Imizu, Toyama 939-0398, Japan

Kazunori Umeo
Cryogenics and Instrumental Analysis Division, N-BARD, Hiroshima University, Higashi-Hiroshima 739-8526, Japan

Shota Nakamura and Shigeo Ohara
Department of Physical Science and Engineering, Graduate School of Engineering, Nagoya Institute of Technology, Nagoya 466-8555, Japan

The rare-earth chiral compound DyNi₃Ga₉ with trigonal structure shows successive phase transitions at 10, 9, 5.5, and 2.5 K. We previously reported that the transverse elastic modulus C_{66} exhibits significant softening toward $T_Q = 10$ K and the phase transition at T_Q is ferroquadrupolar ordering due to the quasidegenerate quartet under a crystal electric field (CEF). To investigate the order parameter and magnetic field-temperature phase diagrams of the ferroquadrupolar ordering, we performed ultrasonic measurements under magnetic fields. T_Q decreases drastically at low fields in the magnetic field in the c plane. In contrast, T_Q remains even at high fields in the field along the c axis. We found anisotropic and complex phase diagrams, and this anisotropy of the diagrams originates from the field dependences of the CEF energies and a quadrupole interaction. From our calculated results, we propose that the order parameter of the ferroquadrupolar ordering will be the electric quadrupole O_{xy}. There are first-order successive phase transitions in the field sweep in the c plane, and a magnetic-field-induced phase appears in the phase diagram for the a axis.

I. INTRODUCTION

Materials with structural chirality have received attention for their novel physical properties. An asymmetric spin interaction, the so-called Dzyaloshinskii-Moriya (DM) interaction, plays an important role in these compounds in addition to a symmetric spin interaction, such as the Ruderman-Kittel-Kasuya-Yosida (RKKY) interaction [1]. Chiral helimagnets, which have left- or right-handedness of a helical magnetic structure, have been intriguingly studied in chiral compounds, such as MnSi, CsCuCl₃, CrNb₃S₆, and YbNi₃Al₉ [2–9]. Moreover, a chiral magnetic soliton lattice state was also reported in CrNb₃S₆ and Yb(Ni₁₋ₓCuₓ)₃Al₉ [6,8].

Meanwhile, in rare-earth compounds with localized f electrons, fascinating physical properties originating from the orbital degrees of freedom, such as multipolar ordering, are

expected from $4f$ electronic states under a crystal electric field (CEF) [10,11]. In order to study the quadrupole degrees of freedom, the ultrasonic measurement is a powerful tool [12–17]. Recently, the rare-earth chiral compounds $R\mathrm{Ni}_3X_9$ (R = rare earth; X = Al and Ga) with the trigonal ErNi₃Al₉-type structure (space group $R32$) have attracted much attention as candidates for investigating chiral physical properties affected by the quadrupole degrees of freedom [7–9,18–25]. Single crystals of $R\mathrm{Ni}_3X_9$ from R = Gd to Lu can be grown by using the flux method [23].

The Dy-based DyNi₃Ga₉ shows a metallic behavior in the electrical resistivity. The magnetic susceptibility follows the Curie-Weiss law above 60 K. Effective magnetic moments are almost the same value with the free Dy³⁺ ion, suggesting a CEF effect with localized f electrons [24,25]. A phase transition at $T_Q = 10$ K was reported by the specific heat measurement. The temperature T dependences of the magnetization display a tiny anomaly at T_Q. In our previous work, we performed ultrasonic measurements on DyNi₃Ga₉ at zero field and found significant elastic softening of the transverse modulus C_{66} toward T_Q [26].

We carried out CEF analyses for the elastic moduli and the magnetic susceptibility in the nonordered state (NOS). Here,

---

[*]ish@hiroshima-u.ac.jp

[†]Also at Institute for Advanced Materials Research and Cryogenics and Instrumental Analysis Division, N-BARD, Hiroshima University, Higashi-Hiroshima 739-8530, Japan; tsuzuki@hiroshima-u.ac.jp
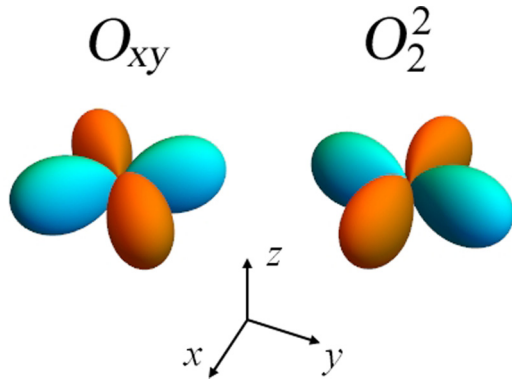
FIG. 1. The schematic pictures of the electric quadrupoles O_{xy} and O_2^2. Orange and cyan on the electric quadrupole express the polar character: positive and negative, respectively.

the 16-fold multiplet of the Dy^{3+} ion (total angular momentum $J = 15/2$) splits into eight Kramers doublets under the trigonal CEF. The data were well reproduced by the obtained CEF level scheme, of which the first excited state at 6 K is sufficiently lower than T_Q, revealing that the ground and first excited doublets form the quasidegenerate quartet. It was also clarified that the softening of the elastic moduli arises from an interlevel quadrupole interaction between the doublets because the Kramers doublets have no quadrupole degeneracy. A quadrupole-quadrupole coupling constant in C_{66} was positive in this analysis. From these results, we proposed that the phase transition at T_Q is ferroquadrupolar (FQ) ordering due to the quasidegenerate quartet [26]. The elastic moduli C_{66} and $(C_{11} - C_{12})/2$ are degenerate in the trigonal symmetry and are the linear responses to the ε_{xy} and $\varepsilon_{xx} - \varepsilon_{yy}$ strains which couple to the electric quadrupoles O_{xy} and O_2^2, respectively. Here, O_{xy} and O_2^2 shown in Fig. 1 are defined as $(J_x J_y + J_y J_x)/2$ and $(J_x^2 - J_y^2)/2$, respectively, where J_x and J_y are components of the total angular momentum. It was suggested that the order parameter of the FQ ordering at T_Q is O_{xy} or O_2^2.

Below T_Q, the spin degrees of freedom within the ground doublet will remain because the FQ ordering at T_Q arises from the quadrupole degrees of freedom among the quasidegenerate quartet. In the specific heat measurement, a small anomaly was detected at $T_N = 9$ K. The T dependence of magnetization along the a axis increases at T_N. An antiferromagnetic (AFM) ordering was proposed as the origin of the phase transition at T_N [25]. With further decreasing T, successive phase transitions at $T_{M1} = 5.5$ K and $T_{M2} = 2.5$ K were also suggested from the specific heat, magnetization, and ultrasonic measurements [25,26].

The magnetic field H dependence of the magnetization at 2 K along the a axis shows metamagnetic transitions at $H_{c1} = 0.05$ T, $H_{c2} = 1.32$ T, $H_{c3} = 3.70$ T, and $H_{c4} = 4.35$ T, and then it saturates above 5 T [25]. Along the b axis, three plateaus were also reported in the magnetization curve, where the b axis is defined as perpendicular to the a axis in the trigonal c plane in this paper. There are metamagnetic transitions at $H_{c1}' = 0.05$ T, $H_{c2}' = 2.22$ T, $H_{c3}' = 3.10$ T, and $H_{c4}' = 5.60$ T along the b axis. In contrast, the magnetization along the c axis increases monotonically up to 5.5 T. The complex H-T phase diagrams were proposed in $DyNi_3Ga_9$.

However, phase boundaries of the FQ ordering are still veiled. In the present work, to investigate the order parameter and the H-T phase diagrams of the FQ ordering, we carried out ultrasonic measurements on $DyNi_3Ga_9$ under magnetic fields.

II. EXPERIMENTAL DETAILS

Single-crystalline $DyNi_3Ga_9$ samples were grown by the flux method. Details of sample preparation and condition were previously reported [25,26]. The T and H dependences of the elastic moduli C_{11}, C_{44}, and C_{66} were measured as a function of T from 0.6 to 30 K and of H up to 14 T using the phase-comparison-type pulse echo method [27]. The modulus C_{11} is the longitudinal mode propagating along the a axis. The transverse moduli C_{44} and C_{66} are modes propagating along the a axis with the polarization direction along the c axis and in the c plane, respectively. The absolute value of the elastic modulus C was calculated using the relation $C = \rho v^2$, where $\rho = 7.74 \, \mathrm{g/cm^3}$ is the mass density at room temperature and v is the sound velocity in a sample. In this paper, the elastic modulus is represented by a relative change of C, $\Delta C/C$, to easily see each data curve. We used $LiNbO_3$ transducers with a fundamental resonance frequency of about 30 MHz. The specific heat was measured by the relaxation method from 2 to 12 K using a commercial physical property measurement system (Quantum Design). The magnetic field was applied by using a superconducting magnet in both measurements.

III. RESULTS

A. Elastic modulus C_{66} under fields

To clarify the FQ ordered state along $H||a$, $H||b$, and $H||c$, we measured the transverse elastic modulus C_{66} corresponding to the quadrupoles O_{xy} and O_2^2. The T and H dependences of C_{66} under fields are shown in Fig. 2. The T dependence of C_{66} at zero field exhibits significant elastic softening toward T_Q with a more than 8% reduction of the stiffness, as shown in Fig. 2(a). Since huge ultrasonic attenuation emerges below T_Q, ultrasonic pulse echoes disappear. These behaviors are also observed up to 1.1 T, indicating the FQ ordering. At 1.3 T, the significant softening stops at 7.5 K, and then C_{66} hardens down to 2 K. Above 2 T, C_{66} displays a broad minimum in the vicinity of 10 K, and the magnitude of the softening decreases with increasing H up to 10 T. These behaviors can be explained by the CEF model with the quadrupole interaction, as discussed in Sec. IV A in detail. A steplike softening with hysteresis is seen at 4 T.

In the H dependences of C_{66} between 4 and 9.5 K shown in Fig. 2(b), we found significant elastic softening toward the FQ ordering for decreasing field. In the FQ ordered state, C_{66} cannot be measured owing to the ultrasonic attenuation. Above T_Q, there is no clear anomaly in the H sweep. On the other hand, obvious elastic anomalies accompanied by hysteresis are detected at around H_{c1}, H_{c2}, H_{c3}, and H_{c4} below 1.8 K, indicating first-order phase transitions, as shown in Fig. 2(c). These hystereses are consistent with the data in the magnetization [25].

Along $H||b$, significant softening is observed up to 2 T in the T dependences of C_{66}, as shown in Fig. 2(d). In the data at 2.7 T, the softening stops at 5 K, and then C_{66} hardens down to
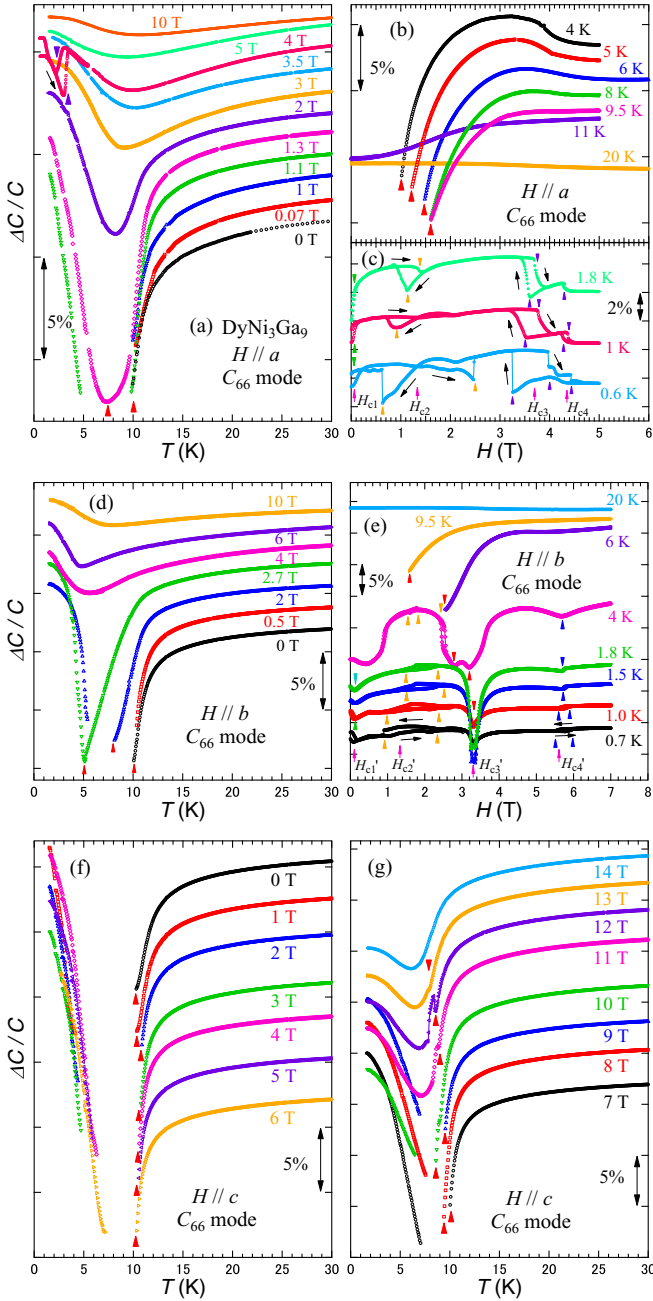
FIG. 2. T and H dependences of the transverse elastic modulus C_{66} along (a)–(c) $H||a$, (d) and (e) $H||b$, and (f) and (g) $H||c$ at various conditions in DyNi$_3$Ga$_9$. We plotted $\Delta C/C$ by adding a constant value to easily see each data curve. The arrows indicate the phase transitions. Pink arrows in the H dependences denote successive phase transitions at H_{c1} (H_{c1}'), H_{c2} (H_{c2}'), H_{c3} (H_{c3}'), and H_{c4} (H_{c4}').

2 K. With further increasing H, the magnitude of the softening decreases, and C_{66} displays a broad minimum in the vicinity of 5 K, as is the case with C_{66} above 2 T along $H||a$.

The FQ phase transition is also detected in the H sweep below T_Q. There is significant elastic softening toward T_Q at 6 and 9.5 K for decreasing field. Below 4 K, we found a sharp downward peak without hysteresis at H_{c3}', suggesting the second-order phase transition. The downward peak at H_{c3}'
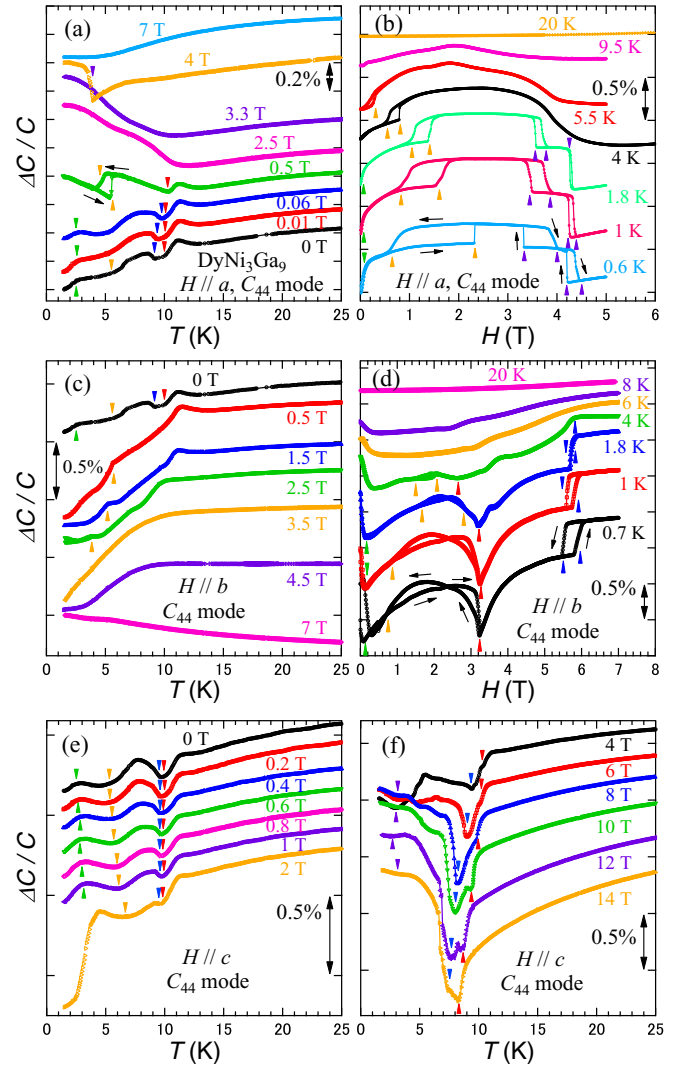

FIG. 3. T and H dependences of the transverse elastic modulus C_{44} along (a) and (b) $H||a$, (c) and (d) $H||b$, and (e) and (f) $H||c$ at various conditions in DyNi$_3$Ga$_9$. The curves are vertically offset for clarity. The arrows indicate the phase transitions.

coincides with the FQ phase boundary in our experimental results. On the other hand, three elastic anomalies accompanied by hysteresis at around H_{c1}', H_{c2}', and H_{c4}' are also observed, indicating that these phase transitions are of the first order.

In the field direction along $H||c$, T_Q is enhanced slightly at low fields and begins to decrease with further increasing H, as shown in Figs. 2(f) and 2(g). Since the ultrasonic attenuation below T_Q becomes small with increasing $H||c$, C_{66} can be measured down to 2 K above 11 T. The H-T phase diagrams of DyNi$_3$Ga$_9$ for the a, b, and c axes are depicted in Sec. III D.

B. Elastic moduli C_{44} and C_{11} under fields

We also measured the elastic moduli C_{44} and C_{11} to investigate the successive phase transitions below T_Q. Figure 3 shows the T and H dependences of the transverse elastic modulus C_{44} under fields in DyNi$_3$Ga$_9$. At zero field, C_{44} softens below 25 K in the T sweep, as shown in Fig. 3(a). Kink anomalies are observed at T_Q and T_N, and then there is

another elastic softening below 8 K with bends at T_{M1} and T_{M2}. Similar behaviors are seen up to 0.06 T along $H||a$. With further increasing H, C_{44} at 0.5 T displays a steplike softening with hysteresis at around 5 K. A sharp downward peak is observed at 4 K in C_{44} at 4 T, and there is no clear anomaly at 7 T. As shown in Fig. 3(b), the H dependences of C_{44} below 1.8 K also exhibit elastic anomalies accompanied by hysteresis at around H_{c1}, H_{c2}, H_{c3}, and H_{c4}. Above T_Q no anomaly is detected in the H sweep.

The T dependences of C_{44} along $H||b$ display a kink anomaly at T_{M1} up to 2.5 T, and T_{M1} decreases with increasing H, as shown in Fig. 3(c). There is no clear anomaly down to 2 K at a selected field above 3.5 T. In the H sweep shown in Fig. 3(d), C_{44} exhibits a downward peak without hysteresis at H'_{c3} and three anomalies accompanied by hysteresis around H'_{c1}, H'_{c2}, and H'_{c4} below 4 K.

Along $H||c$ shown in Figs. 3(e) and 3(f), T_Q and T_N change slightly below 2 T and decrease gradually above 4 T in the T sweep. Elastic anomalies at T_{M1} and T_{M2} are also observed under fields. T_{M1} increases below 6 T, and T_{M2} is hardly changed up to 14 T.

The T and H dependences of the longitudinal modulus C_{11} under fields are shown in Fig. 4. Kink anomalies at T_Q and T_N and a minimum at T_{M1} are observed at low fields along $H||a$, as shown in Fig. 4(a). There is a steplike softening with hysteresis at around 4 K in C_{11} at 1 T, as is the case with C_{44} at 0.5 T. Elastic softening below 25 K at zero field is reduced with increasing H below 2 T. Above 3 T, however, elastic softening is enhanced at elevated fields up to 4 T. The modulus C_{11} at 4 T shows an obvious downward peak at 3.8 K accompanied by hysteresis, indicating the first-order phase transition. No clear phase transition is seen at 5 and 6 T. In the H dependences of C_{11} shown in Figs. 4(b) and 4(c), C_{11} below 3 K exhibits elastic anomalies accompanied by hysteresis at around H_{c1}, H_{c2}, H_{c3}, and H_{c4}. Large hysteresis at around H_{c3} and H_{c4} is not observed in the data at 4 K; however, there is a downward peak without obvious hysteresis.

As shown in Fig. 4(d), two minimums at T_N and T_{M1} are detected in the T dependences of C_{11} along $H||b$. The minimum at T_N becomes broad with increasing H. In contrast, the minimum at T_{M1} displays a sharp peak with hysteresis in the data below 1 T. At 10 T, no anomaly is seen down to 2 K in the T sweep. In the H dependences of C_{11} shown in Fig. 4(e), a downward peak without hysteresis at H'_{c3} and three anomalies accompanied by hysteresis at around H'_{c1}, H'_{c2}, and H'_{c4} are also observed below 5 K, as is the case with C_{66} and C_{44}.

Along $H||c$ shown in Figs. 4(f) and 4(g), T_Q decreases gradually above 4 T in the T sweep. T_{M1} is also observed under fields. C_{11} cannot be measured in the vicinity of 8 T and 8 K because ultrasonic attenuation develops in this region. Since ultrasonic attenuation is linked to the thermodynamic quantities, it is needed to measure ultrasonic attenuation to further investigate the ordered states.

C. Specific heat along $H||a$

The T dependences of the specific heat C_p along $H||a$ are shown in Fig. 5. The sharp peak at T_Q becomes broad at elevated magnetic fields. At 4 T, the peak tends to be unclear, and then C_p increases below 3.8 K.
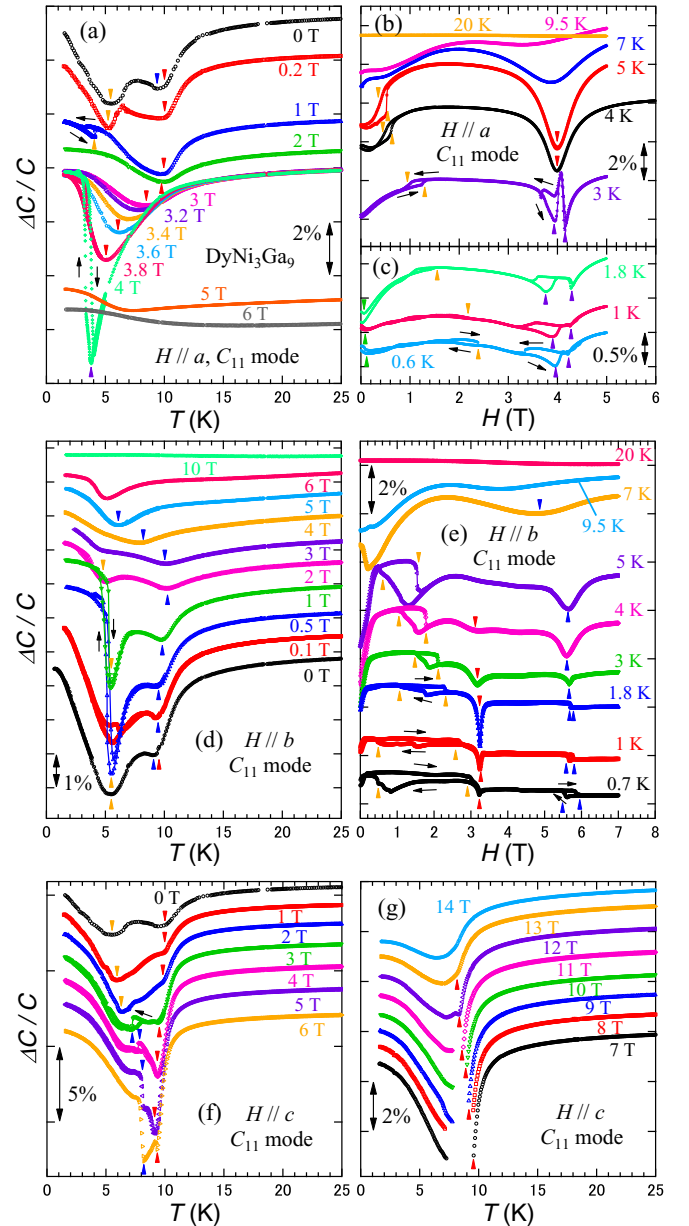

FIG. 4. T and H dependences of the longitudinal elastic modulus C_{11} along (a)–(c) $H||a$, (d) and (e) $H||b$, and (f) and (g) $H||c$ at various conditions in DyNi$_3$Ga$_9$. We plotted $\Delta C/C$ by adding a constant value to easily see each data curve. The arrows indicate the phase transitions.

D. Phase diagram

From these results, we drew the H-T phase diagrams of DyNi$_3$Ga$_9$ for the a, b, and c axes, as shown in Fig. 6. Along $H||a$ shown in Fig. 6(a), the critical field of the FQ (+IAH or +AFM) state increases up to 1.7 T at 8 K, decreases below this temperature, and becomes unclear at 1 T and 4 K. Here, IAH means an incommensurate-antiferromagnetic helix for the following reason. In the ordered state between 9 and 10 K at zero field, the magnetic propagation vector $q = (0, 0, 0.45)$ was obtained by neutron diffraction experiments [25]. Details of those results will be published elsewhere. This suggests that an incommensurate-antiferromagnetic helix structure along
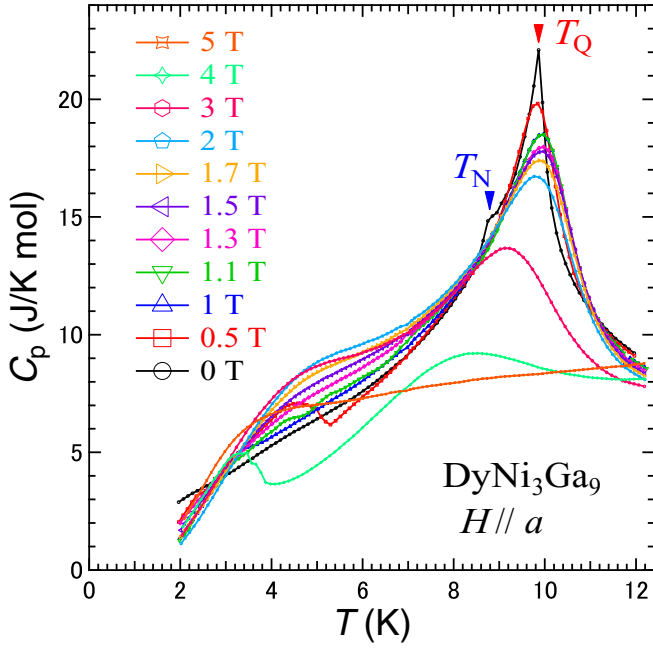
FIG. 5. T dependences of the specific heat C_p along $H||a$ at elevated magnetic fields in DyNi$_3$Ga$_9$.

the c axis coexists with the FQ ordering in this phase. Since the quadrupolar ordered state is affected by the magnetic structure, there is a possibility that quadrupole helix chirality accompanied by chiral magnetic ordering is formed between 9 and 10 K at zero field in DyNi$_3$Ga$_9$. In this case, the AFM ordering at T_N is due to modulation of the magnetic structure because the canted-antiferromagnetic structure was also reported below T_N [25].

In ultrasonic measurements, the successive phase transitions at H_{c1}, H_{c2}, H_{c3}, and H_{c4} can be detected. At these phase boundaries, clear hysteresis is observed, indicating the first-order phase transition. It is also clarified that H_{c3} and H_{c4}

come across at 4 T and 4 K, and a magnetic-field-induced phase (FIP) is formed. The origin of the field-induced phase transition will be discussed in Sec. IV B. The phase boundaries of T_{M1} and T_{M2} correspond to H_{c2} and H_{c1}, respectively. These phase transitions are considered to be magnetic ones (Metamag. and Mag. in the phase diagram) accompanied by a change of the ordered structure because the magnetization increases rapidly at these phase boundaries [25].

For the phase diagram along $H||b$ shown in Fig. 6(b), T_Q slightly increases below 1 T and decreases with further increasing H. Differing from the phase diagram along $H||a$, the phase boundary of T_Q closes around 3.3 T along $H||b$. T_N also increases at low fields, decreases at high fields, and closes around 6 T. At the successive phase transitions at H'_{c1}, H'_{c2}, and H'_{c4}, elastic moduli show clear hysteresis, indicating the first-order phase transition. The phase boundaries of T_{M1} and T_{M2} coincide with H'_{c2} and H'_{c1}, respectively. Along $H||b$, there is no obvious FIP, in contrast to the phase diagram along $H||a$ with the FIP.

We also obtained the phase diagram along $H||c$, as shown in Fig. 6(c). T_Q shows a slight enhancement below 4 T and decreases above this field up to 14 T. The phase boundaries of both T_Q and T_N do not close up to 14 T. We also clarified the phase boundaries of T_{M1} and T_{M2}. T_{M1} becomes unclear in the region in which ultrasonic attenuation develops in C_{11}. Consequently, we clarified the H-T phase diagrams along $H||a$, $H||b$, and $H||c$ and anisotropic phase boundaries of the FQ ordering.

IV. DISCUSSION

A. Order parameter of the FQ ordering

First, we discuss the order parameter of the FQ ordering in DyNi$_3$Ga$_9$. Since significant softening is detected in C_{66}, which corresponds to the electric quadrupoles O_{xy} and O_2^2 in the trigonal symmetry, the order parameter at T_Q is estimated as O_{xy} or O_2^2. To examine which electric quadrupole is the
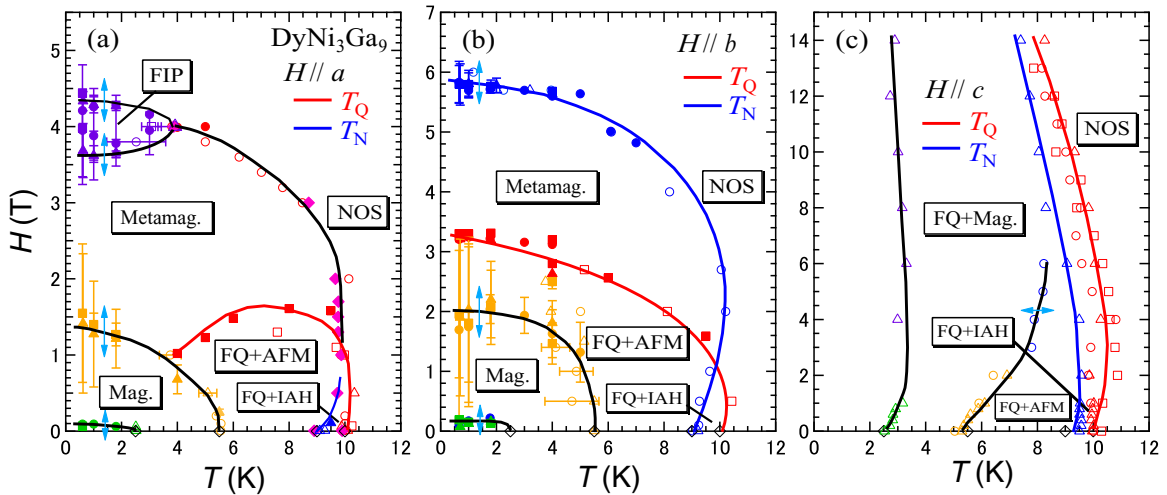

FIG. 6. The H-T phase diagram along (a) $H||a$, (b) $H||b$, and (c) $H||c$ in DyNi$_3$Ga$_9$. The solid curves are guides for the eyes. Solid pink diamonds along $H||a$ represent the phase boundary estimated from C_p. Bidirectional blue arrows point out the first-order phase transition. The middle point of hysteresis is defined as the phase transition, and hysteresis is depicted by an error bar. IAH and FIP indicate an incommensurate-antiferromagnetic helix and a magnetic-field-induced phase, respectively.

order parameter, we performed theoretical calculations of the elastic modulus C_{66} under fields along the principal axes for both O_{xy} and O_2^2 in the NOS. We considered the effective Hamiltonian H_{eff}:

$$H_{eff} = H_{CEF} + H_{Zeeman} + H_Q, \quad (1)$$

$$H_{CEF} = B_2^0 O_2^0 + B_4^0 O_4^0 + B_4^3 O_4^3 + B_6^0 O_6^0$$
$$+ B_6^3 O_6^3 + B_6^6 O_6^6, \quad (2)$$

$$H_{Zeeman} = -g_J \mu_B JH, \quad (3)$$

$$H_Q = -\sum_i g_i O_i \varepsilon_i - \sum_i g_i' \langle O_i \rangle O_i, \quad (4)$$

where ε_i, g_i, g_i', and B_m^n (azimuthal quantum number: $m = 2$, 4, 6 and magnetic quantum number: $n = 0, 3, 6$) are strain, the strain-quadrupole coupling constant, the quadrupole-quadrupole coupling constant, and the CEF parameter, respectively. O_i is equal to either O_{xy} or O_2^2, and H_{Zeeman} is the Zeeman term. The T dependence of C_{66}, $C_{66}(T)$, is represented by the following equation:

$$C_{66}(T) = \frac{-N_0 g_i^2 \chi_s(T)}{1 - g_i' \chi_s(T)} + C_0(T), \quad (5)$$

$$C_0(T) = a + bT^2 + cT^4, \quad (6)$$

where N_0 ($= 4.81 \times 10^{27}$ m^{-3}) is the number density of Dy ions per unit volume at room temperature and χ_s is the so-called strain susceptibility [28]. Details of the calculation are shown in the Supplemental Material [29]. The parameters a, b, and c in Eq. (6) are coefficients for the background stiffness $C_0(T)$ [30]. We adopted B_m^n and other parameters in C_{66} previously reported [26].

Figures 7(a) and 7(b) show the T dependences of the calculated C_{66} for O_{xy} and O_2^2, respectively, along $H||a$. There is a difference between the calculated C_{66} for O_{xy} and O_2^2 because the crystal symmetry in the c plane and the degeneracy between O_{xy} and O_2^2 are broken by applying $H||a$. The calculated C_{66} for O_{xy} exhibits significant softening below 1.5 T, and then the magnitude of the softening decreases with increasing H above 2 T. These behaviors are very similar to the experimental data shown in Fig. 2(a). In contrast, in the calculated C_{66} for O_2^2 shown in Fig. 7(b), significant softening remains up to 3 T, and reduction of the softening is observed above 4 T. From these results, we propose that O_{xy} is a plausible order parameter of the FQ ordering in DyNi$_3$Ga$_9$.

On the other hand, the magnetic field along the c axis does not break the degeneracy between O_{xy} and O_2^2. The calculated C_{66} for O_{xy} and O_2^2 exhibit the same behaviors. As shown in Fig. 7(c), the significant softening appears even at 10 T, and then the calculated C_{66} displays a broad minimum in the vicinity of 4 K above 12 T. These behaviors are quite close to the experimental results along $H||c$ shown in Figs. 2(f) and 2(g). The reason why the calculated C_{66} shows such anisotropic behaviors will be discussed in Sec. IV B.

The FQ ordering must be accompanied by a macroscopic strain or distortion below T_Q. To investigate these things, we carried out a powder x-ray diffraction experiment below and above T_Q. However, we did not succeed in detecting any indication of spontaneous strain, such as splitting or broadening of diffraction peaks. There is a possibility that the magnitude
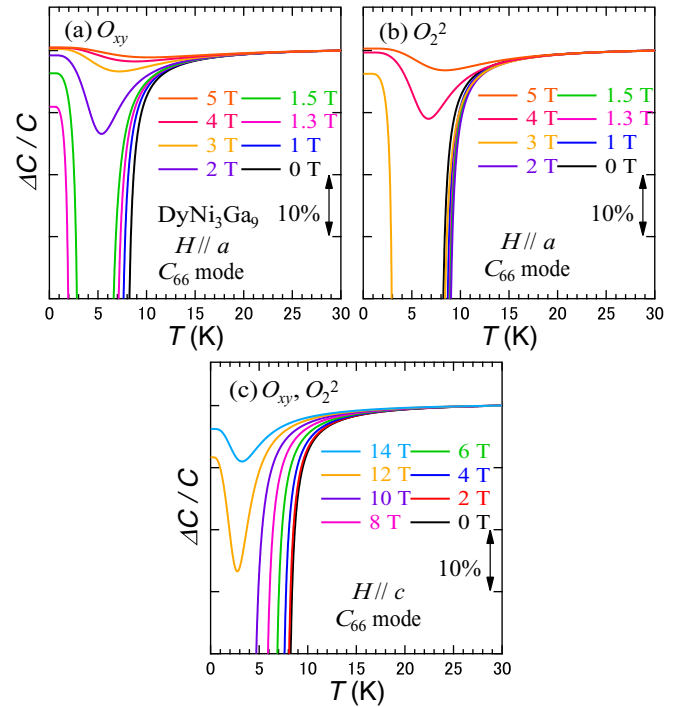

FIG. 7. T dependences of the calculated C_{66} for (a) O_{xy} along $H||a$, (b) O_2^2 along $H||a$, and (c) O_{xy} and O_2^2 along $H||c$.

of the spontaneous macroscopic strain is smaller than the resolution of our x-ray diffraction. We are planning to perform a thermal expansion measurement by using the three-terminal capacitance method in order to determine crystal-symmetry lowering below T_Q.

B. Anisotropic phase diagram

Hereafter, we focus on the origin of anisotropic phase diagrams in DyNi$_3$Ga$_9$. Since the FQ ordering originates from the quasidegenerate quartet under the CEF, the CEF states under fields may play a central role in the FQ ordering. We calculated the H dependences of the CEF energies by using Eqs. (2) and (3), as shown in Fig. 8. Here, the CEF level scheme in zero field is the ground doublet Γ_6, the first excited doublet Γ_{45} at 6 K, the second excited doublet Γ_6 at 11 K, the third excited doublet Γ_6 at 33 K, and so on [26]. The wave functions of the quasidegenerate quartet were also reported.

Along $H||a$, the ground-state doublet Γ_6 starts to possess the quadrupole interaction of O_{xy} and O_2^2 because wave functions of the $4f$ electronic states are mixed by the Zeeman interaction under $H||a$. However, the ground doublet at 0 K in zero field splits monotonically with increasing H due to the Zeeman interaction, as shown in Fig. 8(a). This means that the quadrupole interaction becomes weak with increasing H; thus, the FQ ordered phase exists only at low fields.

Along $H||b$, shown in Fig. 8(b), in contrast, the ground doublet Γ_6 has no quadrupole interaction of O_{xy} and O_2^2, although the energy splitting within the ground doublet is small, and a level crossing is seen at around 12 T. An excited state which has interlevel quadrupole interaction with the ground state separates from the ground state with increasing H. This situation for the interlevel quadrupole interaction is
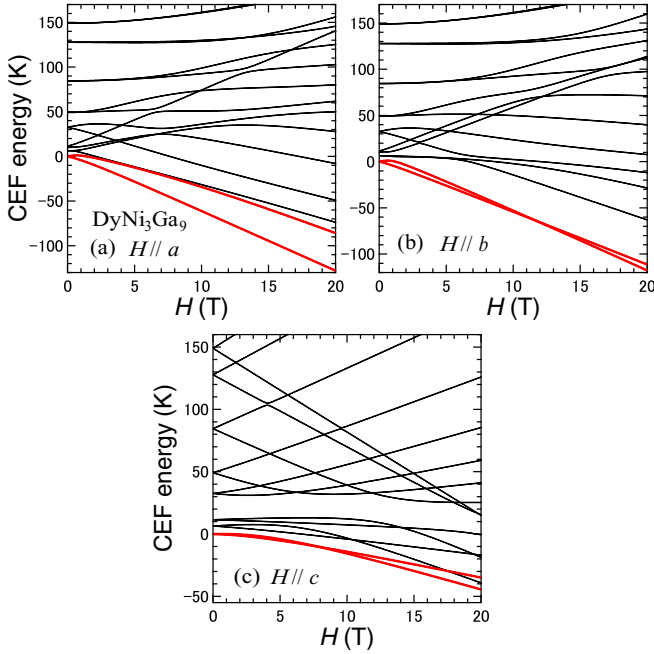
FIG. 8. The H dependences of the calculated CEF energies along (a) $H \| a$, (b) $H \| b$, and (c) $H \| c$. The ground doublet is depicted by the red solid curves.

similar to the calculation along $H \| a$, suggesting that the FQ phase boundary closes at low field.

Meanwhile, along $H \| c$, the ground doublet Γ_6 possesses the quadrupole interaction of O_{xy} and O_2^2. The two states of the ground doublet split slightly below 4 T, reapproach above this field, and show a level crossing at around 8 T, as shown in Fig. 8(c). Above 10 T, the two states split monotonically with increasing H, meaning that the quadrupole interaction begins to decrease above this field. Therefore, the magnitude of the softening decreases above 10 T in the experimental data, shown in Fig. 2(g). As remarked above, the experimental data of C_{66} under fields can be explained by the CEF effect with the quadrupole interaction. As a consequence, anisotropic H-T phase diagrams of the FQ ordering are caused by the H dependences of the CEF energies and the quadrupole interaction.

We carried out a mean-field calculation for the magnetization at 2 K along $H \| a$ by taking into account both quadrupole and spin exchange interactions assuming two sublattices in order to reproduce H_{c1}, H_{c2}, H_{c3}, and H_{c4} [25,31]. The parameters for intersublattice exchange interactions were chosen to reproduce T_Q and T_N. However, the magnetization at 2 K along $H \| a$ could not be explained by the mean-field calculation, although there may be uncertainties, such as the possibility of other higher-order multipolar interactions, optimization of CEF parameters, and the definition of sublattices. DyNi$_3$Ga$_9$ with no inversion symmetry has the DM interaction in addition to the RKKY interaction. The energy scale of the DM interaction is estimated to be several kelvins at most because the chiral helical magnetic structure of the isomorphic compound Yb(Ni$_{1-x}$Cu$_x$)$_3$Al$_9$ is broken by the magnetic field along the a axis below 1 T, and then it changes to a forced ferromagnetic state above this field [8,23]. In addition, the magnitude of the DM interaction in CrNb$_3$S$_6$, which also has a chiral

helical magnetic structure, was theoretically calculated to be 2.9 K [32]. The complex H-T phase diagrams in DyNi$_3$Ga$_9$, especially at low fields, might originate from cooperation and/or competition between the RKKY interaction including the quadrupole interaction and the DM interaction.

We found the FIP around 4 T and below 4 K in the H-T phase diagram for the a axis, as shown in Fig. 6(a). The FQ ordered state is already broken at 4 T. At this phase boundary, the magnetization curve at 2 K displays metamagnetic behavior, suggesting a magnetic phase transition [25]. Since large hysteresis is detected in all moduli and the magnetization, the phase transition is of the first order. In the longitudinal modulus C_{11} shown in Fig. 4(a), elastic softening is enhanced in the vicinity of the FIP boundary, and the magnitude of the softening is about 7% at 4 T. C_{11} is the response to the strain ε_{xx} and is affected by elastic behaviors of the bulk modulus C_B and $(C_{11} - C_{12})/2$ in the trigonal symmetry. However, no enhancement of the softening in the vicinity of 4 T is expected by the data in Fig. 2(a) and the calculation in Fig. 7(b) for $(C_{11} - C_{12})/2$. This suggests that the FIP transition is related to a phase transition accompanied by a change in the bulk modulus.

Generally, coupling between $4f$ electronic states and the strain is considered to be an effect of electric quadrupoles in the localized system. The quadrupole helix chirality might occur in DyNi$_3$Ga$_9$, as mentioned above. Meanwhile, no space-inversion symmetry of the Dy site exists in this compound. In addition, the magnetic field breaks time-reversal symmetry. Recently, theoretical studies of electric and magnetic toroidal multipoles were reported, such as the results in Ref. [33], by considering a parity mixing. As for FIP, an even-parity multipole which couples to the strain of the bulk modulus ε_B with an A_1 totally symmetric irreducible representation may affect the phase transition. On the other hand, since DyNi$_3$Ga$_9$ has a quasidegenerate ground quartet, an effect of higher-order multipolar interactions may exist. In future works, it will be necessary to investigate the influence of higher-order multipolar interactions including electric and magnetic toroidal multipoles in addition to the DM interaction to understand the complex H-T phase diagrams in DyNi$_3$Ga$_9$ [8].

V. CONCLUSION

We measured elastic moduli under magnetic fields in the trigonal chiral compound DyNi$_3$Ga$_9$, which shows FQ ordering at T_Q and successive phase transitions. The significant elastic softening of C_{66} toward T_Q, due to the quadrupolar interaction of the quasidegenerate quartet under the CEF, is reduced by applying $H \| a$ and $H \| b$ even at low fields. In contrast, T_Q survives up to 14 T along $H \| c$. Ultrasonic measurements under fields revealed the anisotropic and complex H-T phase diagrams. We clarified that the FQ phase boundaries are caused by the H dependences of the CEF energies and the quadrupole interaction. A plausible order parameter of the FQ ordering is O_{xy} from our calculation. Successive phase transitions were detected in the H dependences of the elastic moduli. We found a magnetic-field-induced phase along $H \| a$, whose longitudinal modulus C_{11} related to the bulk modulus exhibits enhancement of the softening.

ACKNOWLEDGMENTS

[1] Y. Togawa, Y. Kousaka, K. Inoue, and J. Kishine, J. Phys. Soc. Jpn. **85**, 112001 (2016).

[2] Y. Ishikawa, K. Tajima, D. Bloch, and M. Roth, Solid State Commun. **19**, 525 (1976).

[3] A. E. Petrova and S. M. Stishov, J. Phys.: Condens. Matter **21**, 196001 (2009).

[4] Y. Kousaka, H. Ohsumi, T. Komesu, T. Arima, M. Takata, S. Sakai, M. Akita, K. Inoue, T. Yokobori, Y. Nakao, E. Kaya, and J. Akimitsu, J. Phys. Soc. Jpn. **78**, 123601 (2009).

[5] T. Moriya and T. Miyadai, Solid State Commun. **42**, 209 (1982).

[6] Y. Togawa, Y. Kousaka, S. Nishihara, K. Inoue, J. Akimitsu, A. S. Ovchinnikov, and J. Kishine, Phys. Rev. Lett. **111**, 197204 (2013).

[7] R. Miyazaki, Y. Aoki, R. Higashinaka, H. Sato, T. Yamashita, and S. Ohara, Phys. Rev. B **86**, 155106 (2012).

[8] T. Matsumura, Y. Kita, K. Kubo, Y. Yoshikawa, S. Michimura, T. Inami, Y. Kousaka, K. Inoue, and S. Ohara, J. Phys. Soc. Jpn. **86**, 124702 (2017).

[9] R. Aoki, Y. Togawa, and S. Ohara, Phys. Rev. B **97**, 214414 (2018).

[10] H. Sato, H. Sugawara, Y. Aoki, and H. Harima, in *Handbook of Magnetic Materials*, edited by K. H. J. Buschow (North Holland, Amsterdam, 2009), Vol. 18, Chap. 1.

[11] T. Onimaru and H. Kusunose, J. Phys. Soc. Jpn. **85**, 082002 (2016).

[12] Y. Nemoto, T. Yamaguchi, T. Horino, M. Akatsu, T. Yanagisawa, T. Goto, O. Suzuki, A. Dönni, and T. Komatsubara, Phys. Rev. B **68**, 184109 (2003).

[13] I. Ishii, H. Muneshige, Y. Suetomi, T. K. Fujita, T. Onimaru, K. T. Matsumoto, T. Takabatake, K. Araki, M. Akatsu, Y. Nemoto, T. Goto, and T. Suzuki, J. Phys. Soc. Jpn. **80**, 093601 (2011).

[14] I. Ishii, H. Muneshige, S. Kamikawa, T. K. Fujita, T. Onimaru, N. Nagasawa, T. Takabatake, T. Suzuki, G. Ano, M. Akatsu, Y. Nemoto, and T. Goto, Phys. Rev. B **87**, 205106 (2013).

[15] T. Yanagisawa, T. Goto, Y. Nemoto, R. Watanuki, K. Suzuki, O. Suzuki, and G. Kido, Phys. Rev. B **71**, 104416 (2005).

[16] Y. Nakanishi, S. Takuo, M. Motokawa, T. Matsumura, Y. Nemoto, H. Hazama, T. Goto, and T. Suzuki, Phys. Rev. B **64**, 184434 (2001).

[17] I. Ishii, T. Mizuno, K. Takezawa, S. Kumano, Y. Kawamoto, T. Suzuki, D. I. Gorbunov, M. S. Henriques, and A. V. Andreev, Phys. Rev. B **97**, 235130 (2018).

[18] R. E. Gladyshevskii, K. Cenzual, H. D. Flack, and E. Parthe, Acta Crystallogr., Sect. B **49**, 468 (1993).

[19] Y. Lutsyshyn, Y. Tokaychuk, V. Davydov, and R. Gladyshevskii, Chem. Met. Alloys **1**, 303 (2008).

[20] T. Yamashita, S. Ohara, and I. Sakamoto, J. Phys. Soc. Jpn. **80**, SA080 (2011).

[21] T. Yamashita, R. Miyazaki, Y. Aoki, and S. Ohara, J. Phys. Soc. Jpn. **81**, 034705 (2012).

[22] S. Ohara, T. Yamashita, Y. Mori, and I. Sakamoto, J. Phys.: Conf. Ser. **273**, 012048 (2011).

[23] S. Ohara, S. Fukuta, K. Ohta, H. Kono, T. Yamashita, Y. Matsumoto, and J. Yamaura, JPS Conf. Proc. **3**, 017016 (2014).

[24] L. S. Silva, S. G. Mercena, D. J. Garcia, E. M. Bittar, C. B. R. Jesus, P. G. Pagliuso, R. Lora-Serrano, C. T. Meneses, and J. G. S. Duque, Phys. Rev. B **95**, 134434 (2017).

[25] H. Ninomiya, Y. Matsumoto, S. Nakamura, Y. Kono, S. Kittaka, T. Sakakibara, K. Inoue, and S. Ohara, J. Phys. Soc. Jpn. **86**, 124704 (2017).

[26] I. Ishii, K. Takezawa, T. Mizuno, S. Kamikawa, H. Ninomiya, Y. Matsumoto, S. Ohara, K. Mitsumoto, and T. Suzuki, J. Phys. Soc. Jpn. **87**, 013602 (2018).

[27] T. J. Moran and B. Lüthi, Phys. Rev. **187**, 710 (1969).

[28] B. Lüthi, in *Dynamical Properties of Solids*, edited by G. K. Horton and A. A. Maradudin (North-Holland, Amsterdam, 1980), Chap. 4.

[29] See Supplemental Material at http://link.aps.org/supplemental/10.1103/PhysRevB.99.075156 for calculation of the elastic modulus under the crystal electric field.

[30] M. Nohara, T. Suzuki, Y. Maeno, T. Fujita, I. Tanaka, and H. Kojima, Phys. Rev. B **52**, 570 (1995).

[31] S. Kamikawa, I. Ishii, K. Takezawa, T. Mizuno, T. Sakami, F. Nakagawa, H. Tanida, M. Sera, T. Suzuki, K. Mitsumoto, and X. Xi, Phys. Rev. B **96**, 155131 (2017).

[32] M. Shinozaki, S. Hoshino, Y. Masaki, J. Kishine, and Y. Kato, J. Phys. Soc. Jpn. **85**, 074710 (2016).

[33] S. Hayami and H. Kusunose, J. Phys. Soc. Jpn. **87**, 033709 (2018).